



Supersonically sprayed rGO–Zn₂SnO₄ composites as flexible, binder-free, scalable, and high-capacity lithium ion battery anodes



Tae-Gun Kim ^{a,1}, Edmund Samuel ^{a,1}, Bhavana Joshi ^a, Chan-Woo Park ^a, Min-Woo Kim ^a, Mark T. Swihart ^b, Woo Young Yoon ^{c,**}, Sam S. Yoon ^{a,*}

^a School of Mechanical Engineering, Korea University, Seoul 136-713, Republic of Korea

^b Department of Chemical & Biological Engineering, University at Buffalo, The State University of New York, Buffalo, NY 14260-4200, USA

^c Department of Materials Science & Engineering, Korea University, Seoul 02841, Republic of Korea

ARTICLE INFO

Article history:

Received 29 March 2018

Received in revised form

11 June 2018

Accepted 19 June 2018

Available online 20 June 2018

Keywords:

Supersonic spraying

Lithium-ion battery

Zn₂SnO₄

Binder-free

Flexible electronics

ABSTRACT

Highly flexible, binder-free, scalable, and high-capacity lithium ion battery anodes were fabricated by ball-milling SnO₂ and ZnO₂ particles to form Zn₂SnO₄/SnO₂ ternary oxide particles that were supersonically sprayed over a large area of a flexible copper foil without using any binders. The addition of rGO promoted uniform distribution of the particles and enhanced the overall performance of the composite anodes, which showed excellent long-term stability and a reversible capacity of 1316 mAh·g⁻¹ at a specific current of 100 mA·g⁻¹ after 100 cycles. The supersonic deposition promoted inter-particle cohesion as well as adhesion of the coating materials onto the flexible substrate. Without added binder, the potential adverse effects of using binders on the electrical properties of the anodes were eliminated. The morphology and composition of the samples were characterized by scanning electron microscopy, transmission electron microscopy, X-ray diffraction, Raman spectroscopy, and X-ray photoelectron spectroscopy. The low-cost and scalable synthesis and deposition methods used here may offer a pathway for achieving commercially viable high-capacity anodes for various flexible electronic devices.

© 2018 Elsevier B.V. All rights reserved.

1. Introduction

Lithium ion batteries (LIBs) are widely used in mobile communication devices, portable electronics, implantable medical devices, and both hybrid and all-electric vehicles [1]. For commercial application, LIBs must satisfy the stringent requirements of safety, stability, cost, recyclability, and compatibility with existing infrastructure, while achieving ever higher energy-to-weight and power-to-weight ratios and a low self-discharge rate [2]. On the other hand, at the research level, high energy density and long-term stability are the major parameters of interest. Graphite has long been used commercially due to its excellent long-term stability and electrical conductivity. However, it suffers from a low Li-storage capacity, with a theoretical maximum value of just

372 mAh·g⁻¹ [3].

Metal oxides have been widely considered as a promising alternative to graphite-based anode materials because of their high thermal stability, ionic-selectivity, and electrochemical stability. The transport of ions within metal oxide nanoparticles (NPs) is superior due to the interstitial and substitutional reaction sites of these NPs, thereby leading to high capacity and rate capability [4,5]. For this reason, various efforts have been made to increase the interfacial area by introducing various micro-nanostructures, hollow structures, sheet-like structures, micro-nanorods, and hierarchical structures [6–11].

Among the various metal oxides, tin oxides deliver a very high specific capacity when employed in LIB anodes [12]. Tin-based materials, such as SnO₂, SnO₂-ZnO, Sn-ZnO, and Zn₂SnO₄, have been used for applications in LIBs, gas sensors, and solar cells [13–15]. Notably, mechanical strain or expansion of the material during Li-insertion is alleviated by using bi-metal oxides. These oxides generally serve as a good buffer because the two different metals react with lithium at different potentials. The reduced burden of stress achieved with bi-metal oxides permits long-term

* Corresponding author.

** Corresponding author.

E-mail addresses: wyoon@korea.ac.kr (W.Y. Yoon), skyoony@korea.ac.kr (S.S. Yoon).

¹ Equal contribution.

stable electrochemical performance of the anodes. For this reason, zinc stannate (Zn_2SnO_4) is considered a good candidate for use in LIB anodes. It combines high galvanostatic theoretical capacity [16], high electrical conductivity, and lower volume expansion compared to single-metal oxides [17].

Despite the advantages described above, complex processes employed for the synthesis of Zn_2SnO_4 NPs and agglomeration of the resulting NPs are often-encountered hurdles to the practical and widespread use of these materials in LIB anodes. Zn_2SnO_4 has been synthesized via a hydrothermal method, which includes a complex post-processing step of cleansing the oxide particles [18,19]. Furthermore, slurry coating is utilized to deposit the synthesized nanoparticles, which requires the use of binders (such as polyvinylidene fluoride, PVDF). In general, binders are considered impurities that diminish the electrochemical properties of the anode. Specifically, the binders slow Li-ion diffusion and deteriorate the overall LIB performance. To prevent this, additives such as carbon black or equivalent substances are used to balance the adverse effect of using binders, which increases the number of fabrication steps and cost. Moreover, binders increase anode mass and volume without increasing Li-ion storage capacity.

Herein, we aim to address the following three major issues: a) the complex synthesis of Zn_2SnO_4 particles, b) agglomeration of these nanoparticles, and c) their deposition on a flexible substrate with good cohesion and adhesion via rapid coating with high throughput. Facile synthesis of the Zn_2SnO_4 particles is achieved by simple ball-milling of SnO_2 and ZnO particles for a sufficient duration [20,21]. Agglomeration of the particles is minimized via addition of rGO, which facilitates uniform distribution of the particles on the rGO sheets. In addition, the use of rGO provides shorter pathways for electron transport in the oxide, which enhances charge transfer from the oxide to the current collector. Lastly, cohesion and adhesion are promoted by supersonic spraying, which involves supersonic impact between the particles and the flexible substrate during deposition. Furthermore, supersonic spraying is vacuumless, rapid, and has high throughput, and is therefore appropriate for mass production on a commercial scale.

2. Experimental procedure

2.1. Preparation of rGO/ Zn_2SnO_4 / SnO_2 composite

Fig. 1 presents a schematic of the steps involved in preparing the rGO/ Zn_2SnO_4 / SnO_2 film. The first step involved ball-milling of SnO_2 (<100 nm avg. Sigma-Aldrich) and ZnO (100 nm, Sigma-Aldrich) powder using a ball-mill (PL-BM5L, AC 220V 50/60HZ, Poong Lim Tech., Korea) with ceramic balls (aluminum silicate) for milling times of 24 and 72 h. The SnO_2 / ZnO powders were combined in a molar ratio of 2:1 (tin oxide (6.028 g) to zinc oxide (1.628 g)) for ball-milling. Ball-milling of SnO_2 / ZnO produced Zn_2SnO_4 / SnO_2 NPs. The Zn_2SnO_4 / SnO_2 powders ball-milled for various times were dispersed in 40 mL of *N,N*-dimethylformamide (DMF, Reagent Duksan, Korea) along with 0.3 mL of polyacrylonitrile (PAN) solution in DMF (8 wt%) and the mixture was used as a precursor for supersonic spraying. In the supersonic spraying process, compressed air was heated to 250 °C then fed into a converging-diverging De-Laval nozzle at a pressure of 4 bar. The high-velocity gas emerging from the nozzle was directed onto the substrate (nozzle-to-substrate distance: 13 cm) with the dispersion of NPs (with or without rGO) passing through the atomizer at the outlet of the nozzle as shown in Fig. 1 to deposit the film on pre-cleaned battery grade copper foil. The precursor solution was supplied to the atomizer at a flow rate of 1.5 mL min⁻¹ by a syringe-pump (Legato 210, KDS). The traverse speed was 1 cm s⁻¹ and the sample was coated with *n* = 10 passes. The rGO/ Zn_2SnO_4 / SnO_2 films

were deposited from a dispersion containing 0.25 g of rGO (N002-PDR, Angstrom Materials) in addition to the metal oxide NPs. In the supersonic cold spray process, the compressed hot air approaches the substrate at supersonic velocity. However, the substrate remains near room temperature; hence, the process is termed cold spray. Further details of the supersonic cold spray process are presented in our previous report [21]. The cold sprayed films were annealed under argon atmosphere at 700 °C for 60 min after heating at a rate of 3 °C min⁻¹. In the heat treatment process, a small amount of PAN (<1% of the SnZn in the precursor dispersion) was carbonized [21]. The powders ball-milled for 24 and 72 h, and the 72 h/rGO composite sample are denoted as ZTO1, ZTO2, and ZTO3, respectively.

2.2. Electrochemical tests

The annealed samples were punched into circular electrodes (14 mm diameter) and assembled in CR2032 coin-type half-cells for electrochemical testing. A Li sheet was used as the counter electrode, and a microporous polymer separator (Celgard 2400; Celgard, Chungbuk, South Korea) was placed between the two electrodes for electrical isolation. The liquid electrolyte used in the coin cell was composed of 1 M LiPF₆ in a mixture of ethylene carbonate (EC), dimethylcarbonate (DMC), and ethyl methyl carbonate (EMC) (1:1:1 by volume) (PuriEL, Soulbrain, Seongnam, South Korea). The galvanostatic discharge/charge (lithiation/delithiation) data were acquired over a range of 0.01–3 V at 25 °C using a WBCS3000 battery cycler system (WonATech, Seoul, South Korea). The half-cells were subjected to rate tests and long-term cycling tests (at a current density of 100 mA g⁻¹) for 90 and 100 cycles each.

2.3. Physicochemical characterization

The crystallinity of the cold spray coated films on the copper substrate was characterized by X-ray diffraction (XRD, SmartLab, Rigaku). Imaging of the surface morphology and elemental mapping were performed using a scanning electron microscope (FE-SEM, S-5000, Hitachi, Ltd.) and a transmission electron microscope (TEM, JEM 2100F, JEOL, Inc.), along with energy dispersive spectroscopy (EDS). The TEM samples were prepared on copper grids. The chemical bonding in Zn_2SnO_4 / SnO_2 /rGO was probed by Raman spectroscopy (Jasco, NRS-3100). X-ray photoelectron spectroscopy (XPS, Theta Probe Base System, Thermo Fisher Scientific Co.) was employed to evaluate the chemical states of the elements in the films and the overall elemental composition of the film surface.

3. Results and discussion

XRD patterns of the three samples are presented in Fig. 2a. For samples ZTO1, ZTO2, and ZTO3, a mixture of Zn_2SnO_4 and SnO_2 phases was detected based on the SnO_2 / ZnO starting ratio, with no evidence of the ZnO phase, which suggests that ZnO was transformed to Zn_2SnO_4 . The Zn_2SnO_4 is formed due to cold welding of SnO_2 / ZnO during ball-milling. The Zn_2SnO_4 peaks observed at 34.29, 35.9, 41.68, 51.65, 55.11, 63.5, 68.7, and 71.38° correspond to the (311), (222), (400), (422), (511), (440), (620), and (533) planes (JCPDS file no. 24-1470). The SnO_2 peaks at diffraction angles of $2\theta = 26.5, 33.8, 37.5, 57.8, 61.1, 64.2, \text{ and } 66.1^\circ$ correspond to the (110), (101), (200), (002), (310), (112) and (301) planes, respectively (JCPDS 88-0287).

Fig. 2b shows Raman spectra of ZTO1, ZTO2 (Zn_2SnO_4 / SnO_2 ball-milling times of 24 and 72 h respectively), and the ZTO3 (rGO/ Zn_2SnO_4 / SnO_2) composite sample excited by a 532 nm laser. The broad peaks at 1345 and 1578 cm⁻¹ are respectively assigned to the

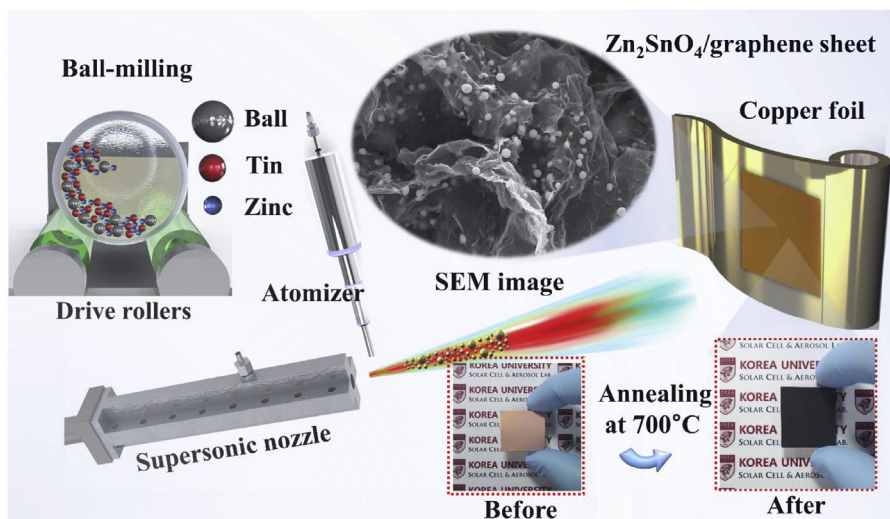


Fig. 1. Schematic showing ball-milling, supersonic spray setup, deposited film on copper foil, and SEM image exhibiting morphology of carbonized composite sample.

defect (D band, sp^3 carbon bonds) and the graphitic states (G band, sp^2 carbon bonds) of the samples. The broad and low-intensity D and G bands for ZTO1 and ZTO2 are attributed to carbonized PAN [22,23]. However, the narrower and distinct D and G bands for ZTO3 are due to the presence of the graphene sheets.

Fig. 3 shows SEM micrographs of the Zn_2SnO_4/SnO_2 particles and $rGO/Zn_2SnO_4/SnO_2$ deposited on copper foil via the supersonic cold spray process. Fig. 3a and b shows high-magnification images of the Zn_2SnO_4/SnO_2 samples ball-milled for 24 and 72 h, respectively. As is apparent, the cold spray particles were agglomerated, which may lead to pulverization during the electrochemical process. The high- and low-magnification SEM images of the $rGO/Zn_2SnO_4/SnO_2$ composite sample are shown in Fig. 3c and d. The image of ZTO3, which comprises the bimetallic oxide ball-milled for 72 h and cold sprayed with graphene sheets, showed wrapping of

the Zn_2SnO_4/SnO_2 particles. It is evident that the presence of the graphene sheets limits agglomeration of the particles, which can reduce the strain generated during the lithiation/de-lithiation process. Furthermore, the low-magnification image of ZTO3 shows that the particles were well dispersed, with transparency of the graphene sheets, suggesting that the graphene sheets were also less stacked (better exfoliated) due to the addition of the metal oxide particles [22].

The surface composition of the rGO/Zn_2SnO_4 composite and the oxidation state of the elements were studied by XPS. The survey spectrum of the $rGO/Zn_2SnO_4/SnO_2$ composite (Fig. 4a) confirms the presence of Sn, Zn, C, and O. The Sn 3d spectrum in Fig. 4b shows peaks at 487 and 495.8 eV, corresponding to Sn $3d_{5/2}$ and $3d_{3/2}$, respectively, with a spin-orbit splitting coupling energy of 8.8 eV. The two peaks suggest that Sn is present in two chemical

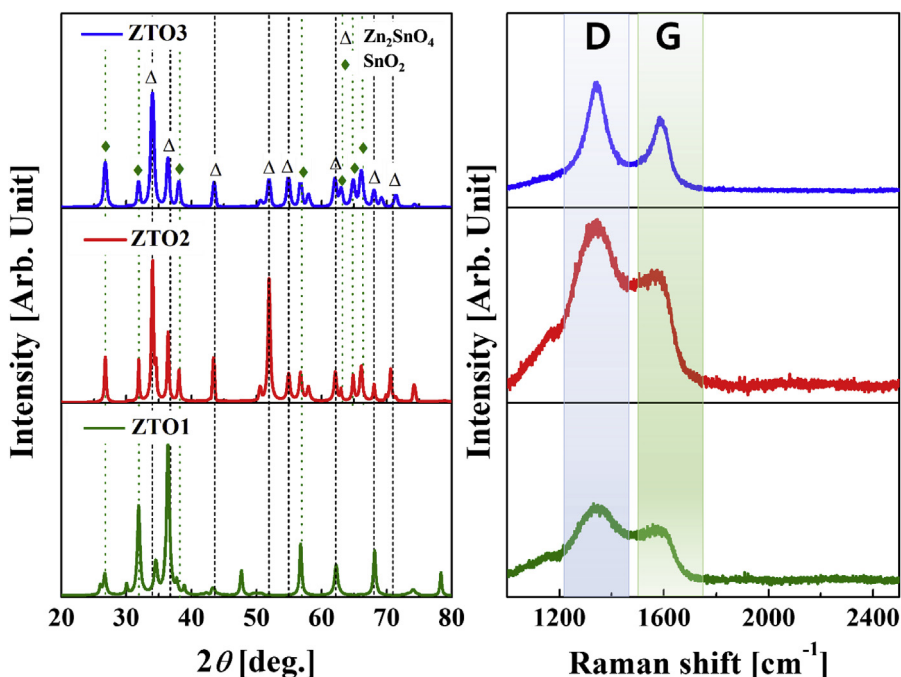


Fig. 2. (a) XRD patterns and (b) Raman spectra of Zn_2SnO_4/SnO_2 (ZTO1 and ZTO2) and $rGO/Zn_2SnO_4/SnO_2$ composite (ZTO3).

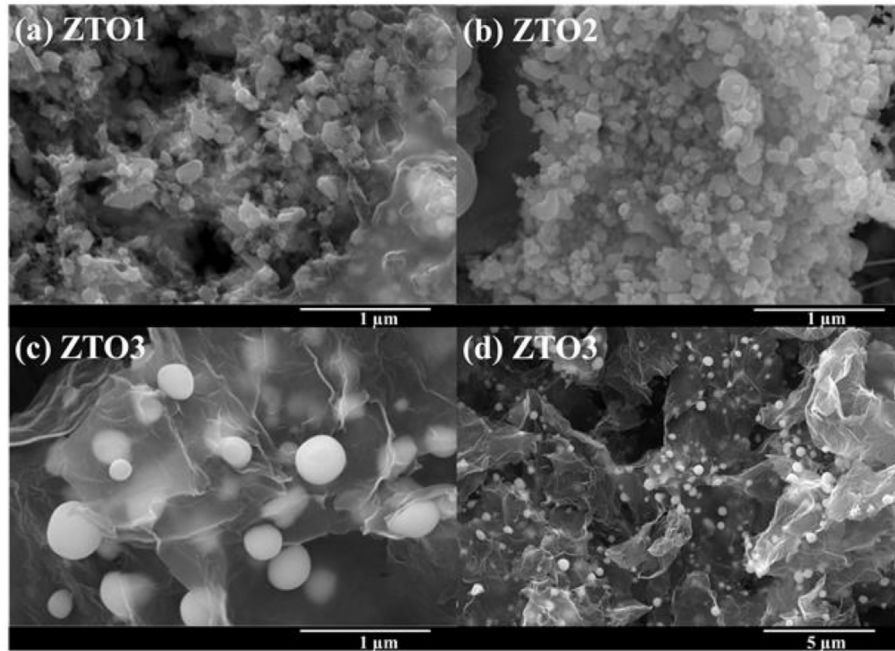


Fig. 3. SEM images of Zn₂SnO₄ and rGO/Zn₂SnO₄: (a) ZTO1, (b) ZTO2, (c) ZTO3 (zoomed view), (d) ZTO3 (zoom out view).

states: Sn²⁺ and Sn⁴⁺. Furthermore, the Zn²⁺ state is indicated by the peaks at 1022.3 and 1045.2 eV, corresponding to Zn 2p_{3/2} and Zn 2p_{1/2} (Fig. 4c). The peak at 285 eV shown in Fig. 4d is the C 1s peak arising from the graphene sheets. The inset in Fig. 4d shows the high-resolution spectrum of oxygen; the peak at 532 eV corresponds to O 1s, plausibly from the Sn-O-Zn or Sn-O-Sn groups.

Morphological and structural analysis of ZTO3 was carried out by TEM. The low-magnification (Fig. 5a) image clearly reveals the

presence of Zn₂SnO₄/SnO₂, along with the graphene sheets. It was also found that these particles were wrapped in the graphene sheets, as indicated by the bright areas. The high-resolution TEM (HRTEM) image of the fabricated rGO/Zn₂SnO₄/SnO₂ electrode in Fig. 5b shows distinct lattice fringes. The blue line shows a lattice spacing of about 0.256 nm, corresponding to the (222) planes of Zn₂SnO₄. The yellow line highlights the fringes at 0.338 nm, attributed to the (110) plane of SnO₂. The SAED pattern (Fig. 5c)

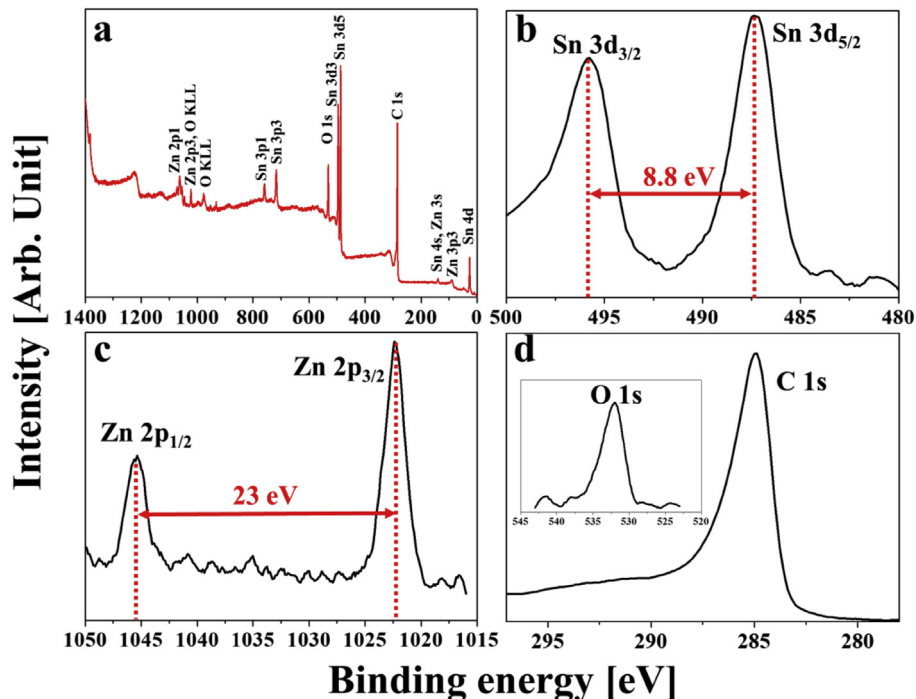


Fig. 4. XPS analysis of rGO/Zn₂SnO₄/SnO₂ (ZTO3) composite sample: (a) XPS survey spectrum, core spectra of (b) Sn 3d, (c) Zn 2p, and (d) O 1s, C 1s, respectively.

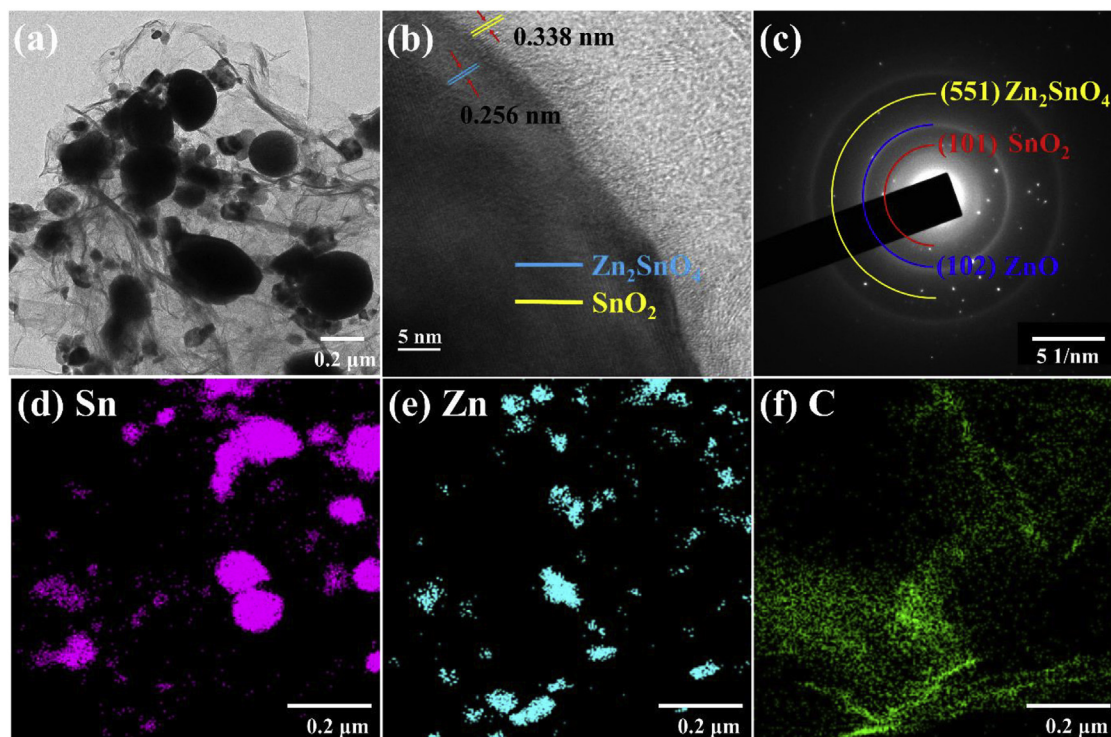


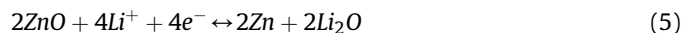
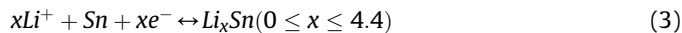
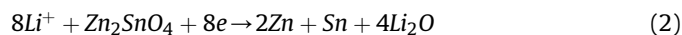
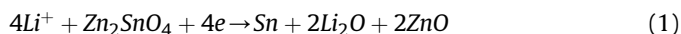
Fig. 5. Transmission electron microscopic analysis of ZTO3, (a) low-magnification TEM image, (b) high-resolution TEM image, (c) SAED ring-pattern, (d)–(f) elemental mapping depicting (d) Sn, (e) Zn, and (f) C.

shows diffraction rings of Zn_2SnO_4 , SnO_2 , and ZnO , corresponding to the (551), (101), and (102) planes, which are well matched with the planes shown in the XRD pattern in Fig. 2a. Elemental mapping images of tin, zinc, and carbon are shown in Fig. 5d–f. The elemental mapping reveals the colocalization of tin and zinc on the graphene sheets.

Fig. 6 a–c display galvanostatic charge–discharge curves acquired over a range of 0.01–3 V at 100 mA g^{-1} . The discharge/charge curves for $N = 1, 2,$ and 100 cycles were acquired to probe the changes in the lithiation and delithiation process during long-term cycling. The galvanostatic curves of the bimetallic oxide active matrix anodes were affected by phase transformation, as depicted in Fig. 6a and b. Although the galvanostatic curves of ZTO2 and ZTO3 did not differ significantly for the first two cycles, the curves of ZTO3 for $N = 100$ demonstrated significantly improved capacity retention. The initial discharge capacities for ZTO1, ZTO2, and ZTO3 were 1527, 2271, and 2174 $\text{mAh} \cdot \text{g}^{-1}$, respectively. However, during the second cycle, the discharge capacities declined, as indicated in Fig. 6a–c; the excess capacity during the initial discharge cycle is partially attributed to irreversible capacity delivered during formation of the solid electrolyte interphase (SEI) layer.

The electrochemical behavior of Zn_2SnO_4 and $rGO/Zn_2SnO_4/SnO_2$ during discharging (lithiation) and charging (delithiation) was complex. Scheme 1 presents an illustration of a plausible mechanism for the complex phenomena occurring during lithiation/delithiation for the ZTO3 case.

In accordance with the above schematic and the galvanostatic charge/discharge profile presented in Fig. 6, the mechanism of the electrochemical lithiation and delithiation processes can be summarized as follows [24]:



Thus, Eqs. (1)–(2) clearly indicate that two mechanisms are possible during the first discharge cycle, which may involve twelve Li ions altogether, yielding 2Sn, 2Zn, 2ZnO, and 6Li₂O. In addition to these decomposition reactions of Zn_2SnO_4 , some complex compound products may also be produced due to formation of the SEI layer. Scheme 1(a) shows the as-prepared half-cell; (b) represents the half-cell during lithiation, which yields metallic Sn and Zn, along with binary metal oxides; (c) shows the thin layer on the anode material, which is the SEI layer, as described earlier. During delithiation, SnO_2 and ZnO are reversibly generated, along with some trapped Li_2O , which may add to the irreversible capacity losses.

The differential capacity (dQ/dV) plot of the discharge cycle for ZTO1 presented in Fig. 6d shows two dominant peaks at 0.45 and 0.23 V. The first two cycles in the long-term cycling test were evaluated at a current density of 100 mA g^{-1} (see Fig. 6d). The stronger peak around 0.45 V was possibly enhanced by the formation of a thick SEI layer. During the first lithiation cycle, Zn_2SnO_4 underwent decomposition. Fig. 6e shows three prominent peaks at 0.44, 0.72, and 0.85 V during the first lithiation cycle. Furthermore, the differential capacity profile for ZTO3 presented in Fig. 6f exhibits multiple peaks and broad characteristics, which suggests alleviation of the volumetric stress during insertion of the lithium

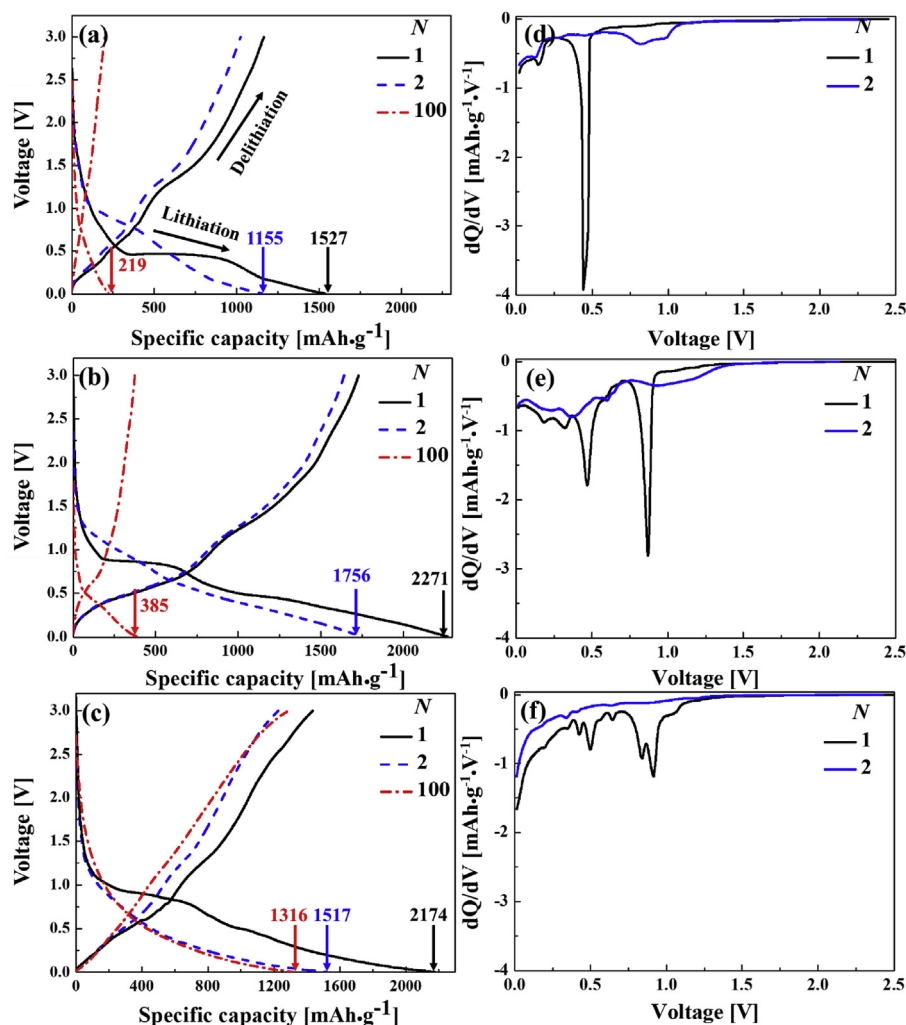


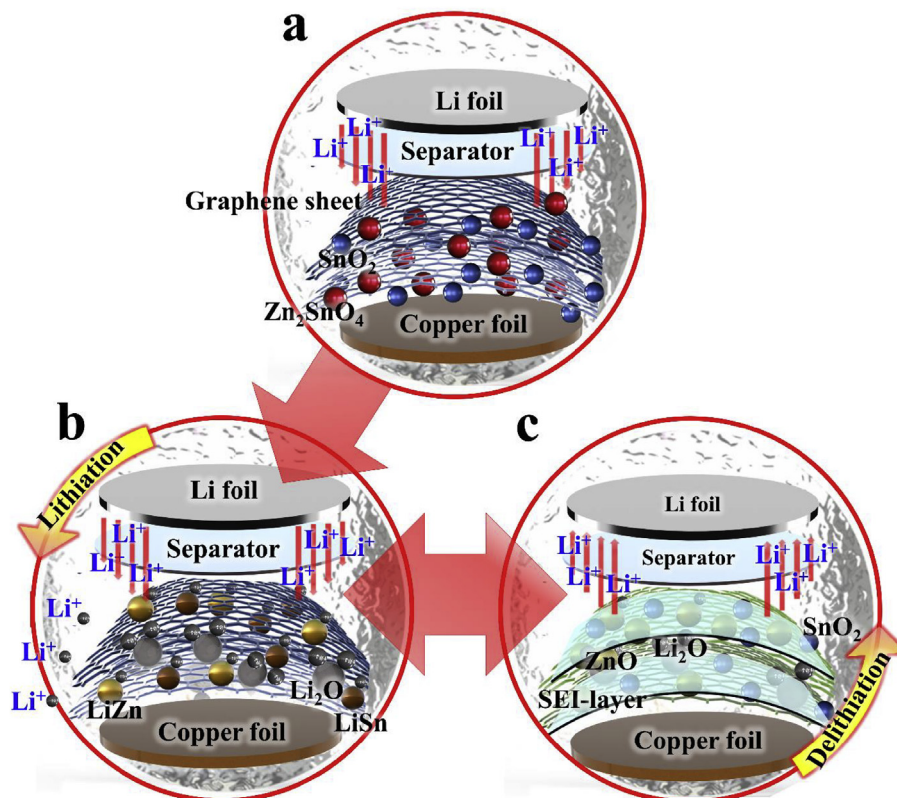
Fig. 6. Discharge/charge profiles (a–c) and variation of differential capacity (d–f) with respect to varying voltage for ZTO1 (a,d), ZTO2 (b,e), and ZTO3 (c,f) samples at low specific current (100 mA g⁻¹).

ions. The reduced stress may be due to the robust framework of the exfoliated graphene sheets and Zn₂SnO₄/SnO₂ particles. Thus, the active material could provide open channels that facilitate fast interstitial diffusion of the lithium ions.

The rate capability and long-term cycling performance of the ZTO1, ZTO2, and ZTO3 samples are shown in Fig. 7a and b, respectively. The current rate capability measurements were carried out by increasing the current density from 50 to 1000 mA g⁻¹ and subsequently decreasing the current density from 1000 mA g⁻¹ to 50 mA g⁻¹. The samples were evaluated at each current rate for ten lithiation and delithiation cycles to test the electrochemical performance of the anode materials. After fifty cycles, reducing the current rate still resulted in a consistent decrease in the specific capacity for ZTO1 and ZTO2. Fig. 7a shows that the capacity of ZTO1 and ZTO2 fell to 200 and 320 mA h g⁻¹ after N = 90 cycles in the current rate electrochemical test. However, ZTO3 exhibited excellent current rate capability and retention. The average reversible capacity of ZTO3 at the respective current densities of 50 and 1000 mA g⁻¹ were 1973 and 764 mA h g⁻¹. Moreover, after N = 90 cycles of the current rate electrochemical test, ZTO3 showed a reversible capacity of 1512 mA h g⁻¹. The superior performance of ZTO3 is due to even distribution of the Zn₂SnO₄/SnO₂ particles over the graphene sheets and the faster charge transfer mechanism.

The long-term cycling performance and coulombic efficiency of

ZTO1, ZTO2, and ZTO3 at a current rate of 100 mA g⁻¹ are shown in Fig. 7b. All three samples show decreasing capacity over the first 30 cycles. However, after that the capacity for ZTO1 and ZTO2 continue to decrease, while that of ZTO3 increases. This behavior may be associated with fragmentation. Fragmentation while maintaining electrical contact with the current collector reduces particle size, and therefore reduces Li-ion diffusion lengths in the oxide material, and can improve capacity at a given rate. In the absence of rGO, fragmentation can lead to loss of electrical contact, and hence loss of performance, but the rGO can allow the fragmented NPs to maintain electrical contact [25,26]. The presence of two metals and their oxides in the Zn₂SnO₄/SnO₂ nanoparticles and the graphene sheets are useful for buffering the volume expansion of the active oxide material during the Li insertion/extraction processes. Further, the bimetallic oxides and the corresponding carbon composite provide a greater number of Li ion storage sites, as illustrated in Eqs. (1)–(6). The ZTO1 and ZTO2 samples exhibited high capacity for tens of cycles during long-term cycling, as depicted in Fig. 7b. However, samples ZTO1 and ZTO2 could not sustain the stress induced by rapid charging and discharging, which led to pulverization and a consistent decline in the capacity (to 293 and 372 mA h g⁻¹, respectively) after 100 cycles. In contrast, the ZTO3 sample showed superior stability due to the synergistic impact of the Zn₂SnO₄/SnO₂ and graphene sheets. As observed from the SEM



Scheme 1. Representation of the half-cell: (a) as-prepared half-cell, (b) cell during discharging, and (c) electrochemical behavior during charging.

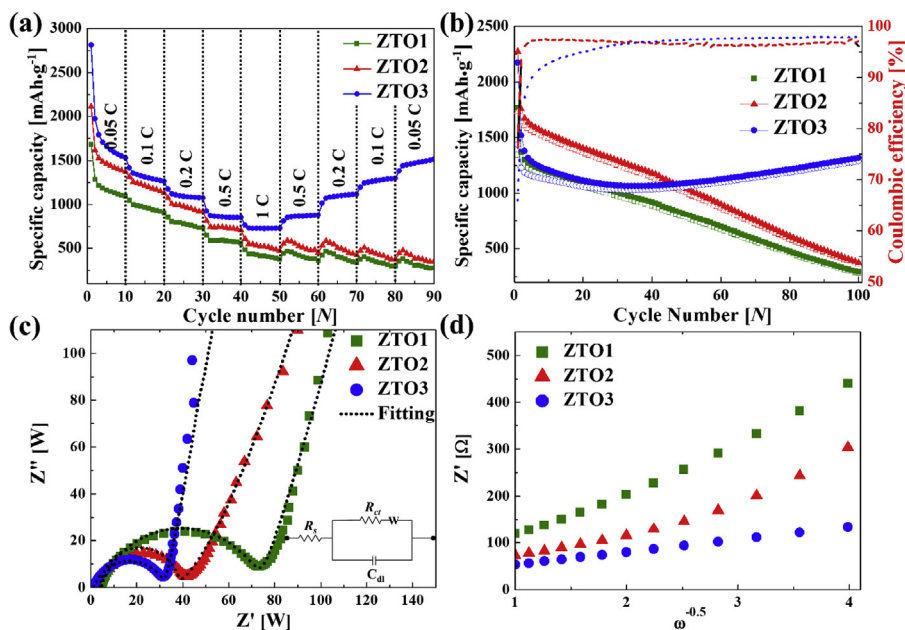


Fig. 7. (a) Rate capability over $N=90$ cycles with variation of the current density and (b) long-term cyclic performance at 100 mA g^{-1} over a voltage range of 0.01–3 V; $1 \text{ C} = 1000 \text{ mA g}^{-1}$. (c) Nyquist plot and (d) relationship between Z' and inverse square root of angular frequency in Warburg diffusion tail region.

images (see Fig. 4c), the Zn₂SnO₄/SnO₂ particles were well wrapped by graphene. Such morphologies provide shorter charge transfer pathways, a thin SEI layer, reduced agglomeration of Zn₂SnO₄/SnO₂, improved maintenance of electrical contact during volume changes, and minimal or no restacking of the graphene sheets. The Coulombic efficiency approaches 100% for ZTO2. The remaining

$\pm 1\text{--}2\%$ variation could be due to trapping of Li-ions and slow structural transformation. Thus, we infer that active material of the electrode is undergoing reversible reactions even after 100 lithiation/de-lithiation cycles [25,26]. Additionally, the availability of Li ion storage sites and the process reversibility remained high for ZTO3, and hence, after 100 cycles, ZTO3 delivered a capacity

Table 1
Comparison of specific capacities reported to date with that from present study.

Composition	Electrode prepared	First Discharge capacity [mAh·g ⁻¹]	First reversible capacity [mAh·g ⁻¹]	Reversible capacity [mAh·g ⁻¹ (N th)	Current rate [mA·g ⁻¹]	Refs.
Zn ₂ SnO ₄	Hydro thermal synthesis	1541	1020	739 (100)	100	[17]
Zn ₂ SnO ₄ /graphene	Hydro thermal synthesis	1367	829	848 (200)	1000	[18]
Zn ₂ SnO ₄ /graphene	Hydro thermal synthesis	1863	1257	726 (50)	300	[19]
Zn ₂ SnO ₄	Hydro thermal synthesis	1750	880	501 (50)	300	[28]
SnO ₂ /ZnO	Hydro thermal synthesis	1540	620	497 (40)	120	[29]
Zn ₂ SnO ₄ /graphene	Hydro thermal synthesis	1764	1069	779(50)	200	[30]
Zn₂SnO₄/graphene	Supersonic spray	2174	1517	1316 (100)	100	Present work

Table 2
Series and charge transfer resistance values determined from Randle's equivalent circuit.

Sample	Series Resistance (<i>R_s</i>) [Ω]	Charge transfer resistance (<i>R_{ct}</i>) [Ω]
ZTO1	0.86	73
ZTO2	0.35	40
ZTO3	0.34	31

retention of 87% (1316 mAh·g⁻¹) relative to the first reversible capacity (1517 mAh·g⁻¹). Table 1 shows a comparison of the significant electrochemical characteristics of the anode (such as the retention capacity and specific capacity) with those recently reported for zinc/tin-based bimetallic oxides.

Fig. 7c shows the Nyquist plots obtained from electrochemical impedance spectroscopic (EIS) analysis of the ZTO1, ZTO2, and ZTO3 electrodes. In all cases, a semicircle was observed in the high–medium frequency range, followed by an inclined line in the lower frequency range. The Nyquist plots were fitted using Zsimp software and the equivalent circuit obtained is depicted in the inset of Fig. 7c. The first *x*-axis intercept of the semicircle represents the

series resistance (*R_s*), which includes the electrolyte resistance and the resistance at the interface of the active material and copper substrate. The second *x*-axis intercept of the semicircle in the medium frequency range is used to calculate the charge transfer resistance (where *R_{ct}* is indicated by the diameter of the semicircle) and *C_{dl}* is the double-layer capacitance developed at the interface of the active material and electrolyte. Table 2 summarizes the resistance values obtained by fitting the Nyquist plots using Randle's equivalent circuit for the ZTO1, ZTO2, and ZTO3 electrodes. The *R_{ct}* values of ZTO2 and ZTO3 decreased relative to ZTO1 due to the enhanced conductivity of Zn₂SnO₄ and the addition of graphene. This decrease in the *R_{ct}* improved the electrochemical kinetics.

The inclined lines in the Nyquist plots at lower frequency represent the Warburg region. To calculate the Li ion diffusion coefficient for the active material during lithiation, the data from the Warburg region were used according to Eq. (7):

$$D = 0.5 \left(\frac{RT}{An^2F^2\sigma_w C} \right)^2 \quad (7)$$

where *D* is the diffusion coefficient, *R* is the gas constant, *T* is the

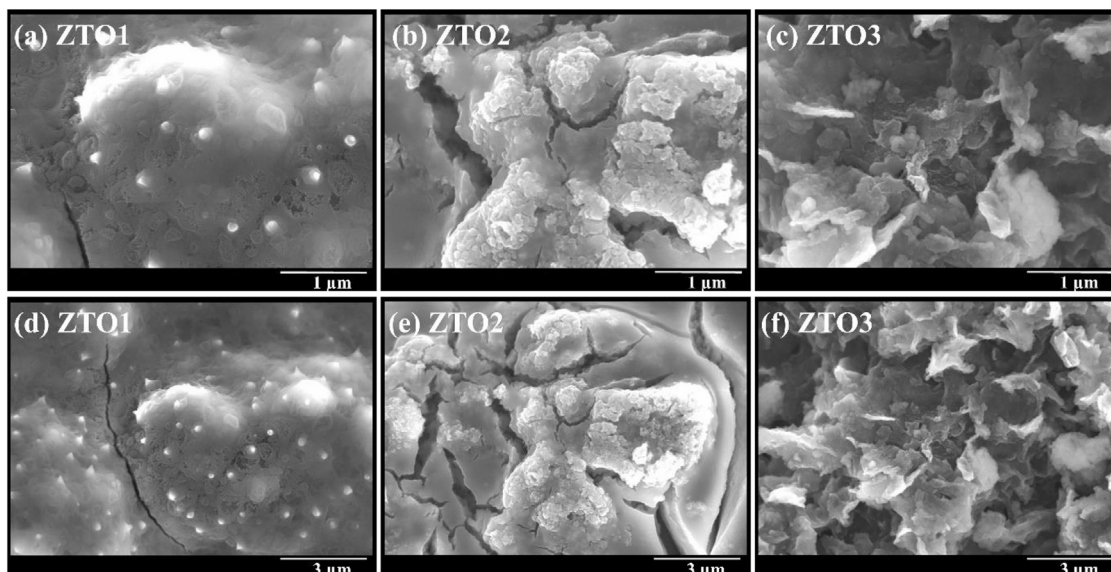


Fig. 8. SEM images of all cases after cycling (a)–(c) low magnification and (d)–(f) high-magnification.

absolute temperature, A is the electrode area, n is the number of electrons involved per molecule, F is Faraday's constant, σ_w is the Warburg coefficient, and C is the concentration. The Warburg coefficient is related to the real impedance (Z') characterized by the "diffusion tail" according to Eq. (8) [27]:

$$Z' = R_s + R_{ct} + \sigma_w \omega^{-0.5} \quad (8)$$

This relation is explored in Fig. 7d, and the slope in each case was used to estimate the diffusion coefficient of the Li ions in the active material during lithiation. The estimated diffusion coefficients for ZTO1, ZTO2, and ZTO3 were 8.6×10^{-10} , 1.7×10^{-9} , and 2.7×10^{-9} , respectively. The estimated diffusion coefficients clearly suggest that Li ion diffusion was improved by anchoring $\text{Zn}_2\text{SnO}_4/\text{SnO}_2$ on the graphene sheets.

The low and high magnification SEM images of Fig. 8 show the morphologies of the ZTO1, ZTO2 and ZTO3 electrodes after cycling. ZTO1 shows pulverized ZnO and SnO particles (initially the particles were bigger as shown in Fig. 3a) with a coating of SEI layer. A similar particle size reduction and SEI layer were observed for ZTO2. However, the pulverized particles are aggregated in absence of graphene sheets. The cracks observed for these two cases could be due the fracture and dissolution of the SEI due to volume expansion and contraction during lithiation and de-lithiation. These morphological characteristics are consistent with the loss of capacity as shown in Fig. 7b. On the contrary, the presence of graphene sheets in ZTO3 does not allow thick SEI formation, extensive aggregation of the particles or catastrophic cracking due to volumetric strain as shown in Fig. 8c. This observation is consistent with the remarkable capacity retention and reversibility of ZTO3 in variable rate and long-term cycling tests.

4. Conclusions

SnO_2 and ZnO_2 particles were ball-milled to form $\text{Zn}_2\text{SnO}_4/\text{SnO}_2$ ternary oxide particles that were supersonically sprayed onto copper foil for use in lithium battery anodes. The fabricated anodes were flexible, scalable, and binder-free, which are desirable features for commercial applications in flexible electronics. Interparticle cohesion and particle–substrate adhesion were ensured via the supersonic spray deposition process. The ball-milled Zn_2SnO_4 particles were wrapped by reduced graphene oxide (rGO) sheets that acted as buffers for volume expansion of the particles. Parametric studies were carried out to identify the optimal formulation of the particles. The combination of Zn_2SnO_4 and rGO yielded the best performance because the rGO sheets promoted uniform distribution of the particles and efficient transfer of lithium. Characterization of the materials confirmed the synthesis of Zn_2SnO_4 via simple ball-milling and the uniform distribution of the particles over the rGO sheets.

Acknowledgement

This research was supported by the Technology Development Program to Solve Climate Changes of the National Research Foundation (NRF) funded by the Ministry of Science, ICT & Future Planning (NRF-2016M1A2A2936760, NRF-2016R1A2B3009481, and NRF-2017R1A2B4005639).

References

- [1] M. Dubarry, C. Truchot, B.Y. Liaw, K. Gering, S. Sazhin, D. Jamison, C. Michelbacher, Evaluation of commercial lithium-ion cells based on composite positive electrode for plug-in hybrid electric vehicle applications. Part

- II. Degradation mechanism under 2 C cycle aging, *J. Power Sources* 196 (2011) 10336–10343.
- [2] J. Jaguemont, L. Boulon, Y. Dubé, A comprehensive review of lithium-ion batteries used in hybrid and electric vehicles at cold temperatures, *Appl. Energy* 164 (2016) 99–114.
- [3] C. Yan, J. Yang, Q. Xie, Z. Lu, B. Liu, C. Xie, S. Wu, Y. Zhang, Y. Guan, Novel nanoarchitected Zn_2SnO_4 anchored on porous carbon as high performance anodes for lithium ion batteries, *Mater. Lett.* 138 (2015) 120–123.
- [4] N. Nitta, F. Wu, J.T. Lee, G. Yushin, Li-ion battery materials: present and future, *Mater. Today* 18 (2015) 252–264.
- [5] H. Mehrer, *Diffusion in Solids: Fundamentals, Methods, Materials, Diffusion-controlled Processes*, Springer Science & Business Media, 2007.
- [6] H.B. Wu, J.S. Chen, H.H. Hng, X.W.D. Lou, Nanostructured metal oxide-based materials as advanced anodes for lithium-ion batteries, *Nanoscale* 4 (2012) 2526–2542.
- [7] Y. Chen, B. Qu, L. Mei, D. Lei, L. Chen, Q. Li, T. Wang, Synthesis of ZnSnO_3 mesocrystals from regular cube-like to sheet-like structures and their comparative electrochemical properties in Li-ion batteries, *J. Mater. Chem.* 22 (2012) 25373–25379.
- [8] J.-F. Duan, S.-C. Hou, S.-G. Chen, H.-G. Duan, Synthesis of amorphous ZnSnO_3 hollow nanoboxes and their lithium storage properties, *Mater. Lett.* 122 (2014) 261–264.
- [9] C.T. Cheria, M. Zheng, M. Reddy, B. Chowdari, C.H. Sow, Zn_2SnO_4 nanowires versus nanoplates: electrochemical performance and morphological evolution during Li-cycling, *ACS Appl. Mater. Interfaces* 5 (2013) 6054–6060.
- [10] Q. Xie, Y. Ma, X. Zhang, L. Wang, G. Yue, D.-L. Peng, $\text{ZnO}/\text{Ni}/\text{C}$ composite hollow microspheres as anode materials for lithium ion batteries, *J. Alloys Compd.* 619 (2015) 235–239.
- [11] X. Sun, W. Si, L. Xi, B. Liu, X. Liu, C. Yan, O.G. Schmidt, In situ-formed, amorphous, oxygen-enabled germanium anode with robust cycle life for reversible lithium storage, *ChemElectroChem* 2 (2015) 737–742.
- [12] X. Zhu, Y. Zhu, S. Murali, M.D. Stoller, R.S. Ruoff, Reduced graphene oxide/tin oxide composite as an enhanced anode material for lithium ion batteries prepared by homogenous coprecipitation, *J. Power Sources* 196 (2011) 6473–6477.
- [13] Y. Zhao, Y. Huang, Q. Wang, K. Wang, M. Zong, L. Wang, W. Zhang, X. Sun, Preparation of hollow Zn_2SnO_4 boxes for advanced lithium-ion batteries, *RSC Adv.* 3 (2013) 14480–14485.
- [14] M.M. Jaculine, C.J. Raj, S.J. Das, Hydrothermal synthesis of highly crystalline Zn_2SnO_4 nanoflowers and their optical properties, *J. Alloys Compd.* 577 (2013) 131–137.
- [15] N. Feng, S. Peng, X. Sun, L. Qiao, X. Li, P. Wang, D. Hu, D. He, Synthesis of monodisperse single crystal Zn_2SnO_4 cubes with high lithium storage capacity, *Mater. Lett.* 76 (2012) 66–68.
- [16] C. Yuan, H.B. Wu, Y. Xie, X.W.D. Lou, Mixed transition-metal oxides: design, synthesis, and energy-related applications, *Angew. Chem. Int. Ed.* 53 (2014) 1488–1504.
- [17] P. Santhoshkumar, K. Prasanna, Y.N. Jo, S.H. Kang, Y.C. Joe, C.W. Lee, Synthesis of highly crystalline octahedron 3D- Zn_2SnO_4 as an advanced high-performance anode material for lithium ion batteries, *Appl. Surf. Sci.* (2018) 514–520.
- [18] L. Qin, S. Liang, X. Tan, A. Pan, $\text{Zn}_2\text{SnO}_4/\text{graphene}$ composites as anode materials for high performance lithium-ion batteries, *J. Alloys Compd.* 692 (2017) 124–130.
- [19] H. Huang, Y. Huang, M. Wang, X. Chen, Y. Zhao, K. Wang, H. Wu, Preparation of hollow Zn_2SnO_4 boxes@C/graphene ternary composites with a triple buffering structure and their electrochemical performance for lithium-ion batteries, *Electrochim. Acta* 147 (2014) 201–208.
- [20] C. Xu, S. De, A.M. Balu, M. Ojeda, R. Luque, Mechanochemical synthesis of advanced nanomaterials for catalytic applications, *Chem. Commun.* 51 (2015) 6698–6713.
- [21] J.-G. Lee, B.N. Joshi, J.-H. Lee, T.-G. Kim, D.-Y. Kim, S.S. Al-Deyab, I.W. Seong, M.T. Swihart, W.Y. Yoon, S.S. Yoon, Stable high-capacity lithium ion battery anodes produced by supersonic spray deposition of hematite nanoparticles and self-healing reduced graphene oxide, *Electrochim. Acta* 228 (2017) 604–610.
- [22] E. Samuel, J.-G. Lee, B. Joshi, T.-G. Kim, M.-w. Kim, I.W. Seong, W.Y. Yoon, S.S. Yoon, Supersonic cold spraying of titania nanoparticles on reduced graphene oxide for lithium ion battery anodes, *J. Alloys Compd.* 715 (2017) 161–169.
- [23] B. Joshi, J.-G. Lee, E. Samuel, H.S. Jo, T.-G. Kim, M.T. Swihart, W.Y. Yoon, S.S. Yoon, Supersonically blown reduced graphene oxide loaded Fe– Fe_3C nanofibers for lithium ion battery anodes, *J. Alloys Compd.* 726 (2017) 114–120.
- [24] L. Qin, S. Liang, A. Pan, X. Tan, Facile solvothermal synthesis of Zn_2SnO_4 nanoparticles as anode materials for lithium-ion batteries, *Mater. Lett.* 141 (2015) 255–258.
- [25] S.J. Rezvani, R. Gunnella, A. Witkowska, F. Mueller, M. Pasqualini, F. Nobili, S. Passerini, A.D. Cicco, Is the solid electrolyte interphase an extra-charge reservoir in Li-Ion batteries? *ACS Appl. Mater. Interfaces* 9 (2017) 4570–4576.
- [26] H. Yue, Z. Shi, L. Wang, X. Li, H. Dong, Y. Yin, S. Yang, Rapid calcination synthesis of $\text{Zn}_2\text{SnO}_4/\text{C}/\text{Sn}$ composites for high-performance lithium ion battery anodes, *J. Alloys Compd.* 723 (2017) 1018–1025.

- [27] A. Amirudin, D. Thieny, Application of electrochemical impedance spectroscopy to study the degradation of polymer-coated metals, *Prog. Org. Coating* 26 (1995) 1–28.
- [28] K. Wang, Y. Huang, H. Huang, Y. Zhao, X. Qin, X. Sun, Y. Wang, Hydrothermal synthesis of flower-like Zn_2SnO_4 composites and their performance as anode materials for lithium-ion batteries, *Ceram. Int.* 40 (2014) 8021–8025.
- [29] M. Ahmad, S. Yingying, H. Sun, W. Shen, J. Zhu, SnO_2/ZnO composite structure for the lithium-ion battery electrode, *J. Solid State Chem.* 196 (2012) 326–331.
- [30] Z. Hou, Z. Chen, M. Jing, H. Yang, G. Li, M. Zhou, RGO–RGONRs– Zn_2SnO_4 composite with three-dimensional hierarchical structure for use in lithium-ion batteries, *J. Electron. Mater.* 47 (2018) 422–429.